Physics of Fluids

Dynamic tensorial eddy viscosity model: Effects of compressibility and of complex geometry

Cite as: Phys. Fluids **34**, 025109 (2022); https://doi.org/10.1063/5.0076341
Submitted: 24 October 2021 • Accepted: 11 January 2022 • Published Online: 08 February 2022

A. Abbà, A. Cimarelli and M. Germano

Phys. Fluids **34**, 025109 (2022); https://doi.org/10.1063/5.0076341 **34**, 025109

Physics of Fluids ARTICLE scitation.org/journal/phf

Dynamic tensorial eddy viscosity model: Effects of compressibility and of complex geometry

Cite as: Phys. Fluids **34**, 025109 (2022); doi: 10.1063/5.0076341
Submitted: 24 October 2021 · Accepted: 11 January 2022 ·

A. Abbà,[1,a)] A. Cimarelli,[2] and M. Germano[3]

AFFILIATIONS

[1]Dipartimento di Scienze e Tecnologie Aerospaziali, Politecnico di Milano, 20156 Milano, Italy
[2]Department of Engineering 'Enzo Ferrari', University of Modena and Reggio Emilia, 41125 Modena, Italy
[3]Department Civil and Environmental Engineering, Duke University, Durham, North Carolina 27708, USA

[a)]Author to whom correspondence should be addressed: antonella.abba@polimi.it

ABSTRACT

A previous paper by Cimarelli *et al.* ["General formalism for a reduced description and modelling of momentum and energy transfer in turbulence," J. Fluid Mech. **866**, 865–896 (2019)] has shown that every decomposition of turbulent stresses is naturally approximated by a general form of tensorial eddy viscosity based on velocity increments. The generality of the formalism is such that it can also be used to give a reduced description of subgrid scalar fluxes. In the same work, this peculiar property of turbulent stresses and fluxes has been dynamically exploited to produce tensorial eddy viscosity models based on the second-order inertial properties of the grid element. The basic idea is that the anisotropic structure of the computational element directly impacts, although implicitly, the large resolved and small unresolved scale decomposition. In the present work, this new class of turbulence models is extended to compressible turbulence. *A posteriori* analysis of flow solutions in a compressible turbulent channel shows very promising results. The quality of the modeling approach is further assessed by addressing complex flow geometries, where the use of unstructured grids is demanded as in real world problems. Also in this case, *a posteriori* analysis of flow solutions in a periodic hill turbulent flow shows very good behavior. Overall, the generality of the formalism is found to allow for an accurate description of subgrid quantities in compressible conditions and in complex flows, independent of the discretization technique. Hence, we believe that the present class of turbulence closures is very promising for the applications typical of industry and geophysics.

I. INTRODUCTION

The old idea of Boussinesq[2] of representing turbulent stress and turbulent dissipation by means of an eddy viscosity has been developed during the years following many distinct directions. The Smagorinsky model,[3] based on the assumptions of isotropic small-scale turbulence in equilibrium with large scales, is the best known example of scalar eddy viscosity. Its dynamic version[4] is addressed to overcome the equilibrium assumption and to better predict wall turbulence, shear, and transitional flow. However, the isotropicity hypothesis is violated not only by large scales, as is evident in complex flows of engineering interest, but also by small scales, usually unresolved in the large eddy simulation (LES) approach, that show strong anisotropicity. Hence, anisotropic, tensorial eddy viscosities have been proposed, mainly empirically, to overcome the isotropicity assumption, in order to combine better with the disalignment of the stress tensor with the Reynolds or the subfilter stress, and in many cases, theoretical arguments have produced anisotropic eddy viscosities depending on unknown constants that dynamically could be better guessed.[5] In particular, we refer here to the approach originally developed by Abbà *et al.*[6] with the goal of removing the limitations related to isotropic eddy viscosity models. There, the subgrid stress tensor was assumed to be proportional to the strain rate tensor through a fourth order symmetric tensor, and a dynamic procedure was developed in order to adjust some undetermined constants with the particular flow.

Non-isotropic grids are usually used in simulations of non-homogeneous flows with the aim to better represent large anisotropic turbulent structures. Often anisotropic grids are imposed, in simulations of turbulent flows of engineering application, by pure geometrical reasons. The use of implicit filtering with anisotropic grids in LES is directly associated with an anisotropic definition of large and small scales. So, the anisotropy of the grid may also be used in turbulence closures to take into account information about the induced anisotropy of subgrid turbulence structures. The first attempt to take into account resolution anisotropy was proposed by Schumann[7] and Zahrai *et al.*,[8] introducing different length scales associated with the face element diagonal. Other proposals have followed, Bardina *et al.*[9] and Abbà *et al.*,[10] based on empirical arguments, which introduced a tensorial filter length.

An approach more fitted to represent the anisotropies induced by the grid has been proposed in a previous paper by Cimarelli *et al.*,[1] where this old problem has been explored in a new way. In the theoretical framework provided by an alternative decomposition of turbulent stresses, a new formalism for their approximation and understanding has been proposed that spontaneously directs to a tensorial turbulent eddy viscosity based on the two-point velocity increments, $\delta u_i = u_i(\mathbf{x}+\delta\mathbf{x}) - u_i(\mathbf{x})$. The formalism strictly connects to numerics, where derivatives are ratios $\delta\mathbf{u}/(\delta\mathbf{x})$ taken at the numerical resolution scale. The derived closure of the tensorial viscosity is based on filtered velocity gradients and on the second order inertial properties of the grid element. The basic idea is that the structure of the computational element impacts the anisotropy of the filtered-out motions, and hence, this information could be leveraged to improve the prediction of subgrid stresses. It is worth noting that a similar idea has been later exploited by Haering *et al.*[11] to develop an anisotropic minimum-dissipation model.

In the present work, we further assess the modeling approach developed in Cimarelli *et al.*[1] with two aims. The first is to extend the modeling approach to compressible turbulence and to test its performance in a turbulent channel. The second is to test the modeling approach in complex flows where the use of unstructured grids is demanded, thus exploiting all the potential of the proposed turbulence closure. For this second purpose, the turbulent flow over periodic hills is considered.

The paper is organized as follows. The filtered equations in the compressible framework and the numerical code are shown in Sec. II, while the closures for subgrid stresses and for subgrid enthalphy and heat fluxes are shown in Sec. III. These turbulence closures are tested and compared with direct numerical simulation (DNS) data in the case of a compressible turbulent channel and of a channel with periodic hills in Secs. IV and V, respectively. This work is closed by final remarks in Sec. VI.

II. THE FILTERED EQUATIONS AND THE NUMERICAL CODE

The filtered Navier–Stokes equations for compressible flows can be written in a dimensionless form as

$$\partial_t \mathbf{U} + \nabla\cdot\left(\mathbf{F}^{\mathrm{a}} - \mathbf{F}^{\mathrm{v}} + \mathbf{F}^{\mathrm{sgs}}\right) = \mathbf{S}, \tag{1}$$

where $\mathbf{U} = [\bar{\rho}, \bar{\rho}\widetilde{\mathbf{u}}^T, \bar{\rho}\widetilde{e}]^T$ are the resolved density of the fluid, the resolved momentum, and the resolved volume specific total energy, respectively. Here, $\bar{\cdot}$ and $\widetilde{\cdot}$ represent the grid filter and the Favre filter operators, respectively, as it will be better explained at the end of this section. In Eq. (1), the advective fluxes are defined as

$$\mathbf{F}^{\mathrm{a}}(\mathbf{U}) = \begin{bmatrix} \bar{\rho}\widetilde{\mathbf{u}} \\ \bar{\rho}\widetilde{\mathbf{u}}\otimes\widetilde{\mathbf{u}} + \dfrac{1}{\gamma Ma^2}\bar{p}\mathscr{I} \\ \bar{\rho}\widetilde{h}\widetilde{\mathbf{u}} \end{bmatrix}, \tag{2}$$

where $\bar{p}$ denotes the filtered pressure, $\bar{\rho}\widetilde{h} = \bar{\rho}\widetilde{e} + \bar{p}$ denotes the resolved enthalpy, Ma is the Mach number, $\gamma = c_p/c_v$ is the heat capacity ratio, and $\mathscr{I}$ is the identity matrix. On the other hand, the viscous fluxes are

$$\mathbf{F}^{\mathrm{v}}(\mathbf{U},\nabla\mathbf{U}) = \begin{bmatrix} 0 \\ \dfrac{1}{Re}\widetilde{\sigma} \\ \dfrac{\gamma Ma^2}{Re}\widetilde{\mathbf{u}}^T\widetilde{\sigma} - \dfrac{1}{\kappa RePr}\widetilde{\mathbf{q}} \end{bmatrix}, \tag{3}$$

where $\widetilde{\sigma}$ and $\widetilde{\mathbf{q}}$ are the momentum and heat diffusive fluxes, respectively, $\kappa = R/c_p$, and Re and Pr are the Reynolds and Prandtl numbers, respectively. Finally, subgrid fluxes are

$$\mathbf{F}^{\mathrm{sgs}}(\mathbf{U},\nabla\mathbf{U}) = \begin{bmatrix} 0 \\ \tau + \varepsilon^{sgs} \\ (\rho h\mathbf{u})^{sgs} - \dfrac{\gamma Ma^2}{Re}\phi^{sgs} + \dfrac{1}{\kappa RePr}\theta^{sgs} \end{bmatrix}, \tag{4}$$

where τ is the subgrid stress tensor, $(\rho h\mathbf{u})^{sgs} = \overline{\rho h\mathbf{u}} - \bar{\rho}\widetilde{h}\widetilde{\mathbf{u}}$ and

$$\varepsilon^{sgs} = \bar{\sigma} - \widetilde{\sigma}, \quad \phi_j^{sgs} = \overline{u_i\sigma_{ij}} - \widetilde{u}_i\widetilde{\sigma}_{ij}, \quad \theta_j^{sgs} = \overline{q_j} - \widetilde{q}_j. \tag{5}$$

These latter contributions to subgrid fluxes will be discussed in Sec. III. Equation (1) is completed by the dimensionless state equation for a perfect gas,

$$\bar{p} = \bar{\rho}\widetilde{T}, \tag{6}$$

where $\widetilde{T}$ is the filtered temperature. The term $\mathbf{S}$ represents a source term

$$\mathbf{S} = \begin{bmatrix} 0 \\ \bar{\rho}\mathbf{f} \\ \bar{\rho}\mathbf{f}\cdot\widetilde{\mathbf{u}} \end{bmatrix}, \tag{7}$$

where $\mathbf{f}$ is a specific, constant in space, driving force. The following constitutive equations must be specified in order to close the system:

$$\widetilde{\sigma}_{ij} = \mu\widetilde{\mathscr{S}_{ij}}^{d}, \quad \widetilde{q}_i = -\mu\partial_i\widetilde{T}. \tag{8}$$

The resolved strain rate tensor is defined as

$$\widetilde{\mathscr{S}_{ij}} = \partial_j\widetilde{u}_i + \partial_i\widetilde{u}_j, \quad \widetilde{\mathscr{S}_{ij}}^{d} = \widetilde{\mathscr{S}_{ij}} - \frac{1}{3}\widetilde{\mathscr{S}_{kk}}\delta_{ij}, \tag{9}$$

where the dynamic viscosity, according to the Sutherland law, is

$$\mu(\widetilde{T}) = \widetilde{T}^{0.7}. \tag{10}$$

The numerical code used in the present work solves the compressible Navier–Stokes equations with the local discontinuous Galerkin (LDG) approach. The code is based on the FEMilaro finite element library, a FORTRAN/MPI library that is publicly available under GPL license at the link https://bitbucket.org/mrestelli/femilaro/wiki/Home. The main features of the numerical method are here reviewed, but for more details, we refer to Tugnoli *et al.*[12]

A Discontinuous finite element space $\mathscr{V}_h$

$$\mathscr{V}_h = \{v_h \in L^2(\Omega) : v_h|_K \in \mathbb{P}^{p_K}(K),\ \forall K \in \mathscr{T}_h\} \tag{11}$$

is defined over a tessellation $\mathscr{T}_h$ composed of non-overlapping tetrahedral elements in the domain Ω. Here, $\mathbb{P}^{p_K}(K)$ denotes the space of polynomial functions of total degree p_K. A modal local discontinuous Galerkin approach[13] is applied to discretize the equations. A hierarchical orthonormal polynomial basis functions ψ_l^K defined on each element K in the finite dimensional space $\mathscr{V}_h$ is used to represent the numerical approximation of a generic variable a,

$$a_h|_K = \sum_{l=0}^{n_\psi(K)} a^{(l)} \psi_l^K. \tag{12}$$

where $a^{(l)}$ is the modal coefficient of the basis functions and $n_\psi(K) + 1$ is the number of basis functions required for the polynomial space $\mathbb{P}^{p_K}(K)$ of degree p_K, defined in $\mathbb{R}^3$ as

$$n_\psi(K) = \frac{1}{6}(p_K+1)(p_K+2)(p_K+3) - 1. \tag{13}$$

In the LDG approach, as explained in van der Bos and Geurts[14] and Abbà *et al.*,[15] the LES filtering operator $\bar{\cdot}$ is equivalent to the projection onto the finite dimensional solution subspace,

$$\bar{a} = \Pi_{\mathscr{V}_h} a, \tag{14}$$

while the Favre filter operator is defined as

$$\overline{\rho a} = \bar{\rho}\tilde{a}. \tag{15}$$

III. THE SUBGRID SCALE MODELS

In Eq. (4), the following terms appear: the subgrid stress tensor

$$\tau_{ij} = \overline{\rho u_i u_j} - \bar{\rho}\tilde{u}_i\tilde{u}_j = \bar{\rho}\left(\widetilde{u_i u_j} - \tilde{u}_i\tilde{u}_j\right), \tag{16}$$

the subgrid enthalpy flux

$$(\rho h u_j)^{sgs} = \overline{\rho h u_j} - \bar{\rho}\tilde{h}\tilde{u}_j = \bar{\rho}\widetilde{h u_j} - \bar{\rho}\tilde{h}\tilde{u}_j \tag{17}$$

and

$$\varepsilon^{sgs} = \bar{\sigma} - \tilde{\sigma}, \quad \phi_j^{sgs} = \overline{u_i\sigma_{ij}} - \tilde{u}_i\tilde{\sigma}_{ij}, \quad \theta_j^{sgs} = \overline{q_j} - \tilde{q}_j. \tag{18}$$

Based on the analysis presented in Pino Martìn *et al.*[16] and Vreman *et al.*,[17] assuming $\bar{\sigma} \simeq \tilde{\sigma}$ and $\bar{\mathbf{q}} \simeq \tilde{\mathbf{q}}$, the terms ϕ^{sgs}, ε^{sgs}, and θ^{sgs} are neglected. Concerning the enthalpy

$$\overline{\rho h} = \bar{\rho}\tilde{h} = \frac{1}{k}\bar{\rho}\tilde{T} + \frac{\gamma Ma^2}{2}(\bar{\rho}\tilde{u}_k\tilde{u}_k + \tau_{kk}), \tag{19}$$

introducing the subgrid heat flux

$$Q_i^{sgs} = \overline{\rho u_i T} - \bar{\rho}\tilde{u}_i\tilde{T} = \bar{\rho}(\widetilde{u_i T} - \tilde{u}_i\tilde{T}) \tag{20}$$

and the turbulent diffusion flux

$$J_i^{sgs} = \overline{u_i u_k u_k} - \bar{\rho}\tilde{u}_i\tilde{u}_k\tilde{u}_k = \bar{\rho}(\widetilde{u_i u_k u_k} - \tilde{u}_i\tilde{u}_k\tilde{u}_k), \tag{21}$$

we obtain

$$(\rho h u_i)^{sgs} = \frac{1}{k}Q_i^{sgs} + \frac{\gamma Ma^2}{2}(J_i^{sgs} - \tilde{u}_i\tau_{kk}). \tag{22}$$

Introducing the generalized central moment[18]

$$\tau(u_i, u_j, u_k) = \bar{\rho}\widetilde{u_i u_j u_k} - \tilde{u}_i\tau_{jk} - \tilde{u}_j\tau_{ik} - \tilde{u}_k\tau_{ij} - \bar{\rho}\tilde{u}_i\tilde{u}_j\tilde{u}_k, \tag{23}$$

the turbulent diffusion flux can be written as

$$J_i^{sgs} = \tau(u_i, u_k, u_k) + 2\tilde{u}_k\tau_{ik} + \tilde{u}_i\tau_{kk}. \tag{24}$$

By this way, subgrid fluxes are reduced to

$$\mathbf{F}^{sgs} = \begin{bmatrix} 0 \\ \tau \\ \frac{1}{k}\mathbf{Q}^{sgs} - \frac{\gamma Ma^2}{2}(\mathbf{J}^{sgs} - \tilde{\mathbf{u}}\tau_{kk}) \end{bmatrix}. \tag{25}$$

Following Cimarelli *et al.*,[1] we model subgrid stresses as

$$\tau_{ij} = -\bar{\rho}\left(\nu_{kj}\partial_k\tilde{u}_i + \nu_{ki}\partial_k\tilde{u}_j\right), \tag{26}$$

where ν_{ki} represents the components of a tensorial subgrid viscosity

$$\nu_{ki} = -\frac{1}{2}\tau(x_h, x_k)\partial_h\tilde{u}_i. \tag{27}$$

The moment

$$\tau(x_h, x_k) = \frac{1}{K_f}\int_{K_f}(\xi_k - x_k)(\xi_h - x_h)d\boldsymbol{\xi} \tag{28}$$

is a tensor related to the inertial tensor of the filter volume, and it is representative of the anisotropy of computational grid, see Cimarelli *et al.*[1] and Haering *et al.*[11] Here, $\mathbf{x}$ is the position of the Gauss nodes where the solution is located in space using quadrature formula, and K_f is the portion of the element grid volume pertinent to each Gauss node. This moment is here computed numerically by

$$\tau(x_h, x_k) = \frac{1}{Kn_\psi^2(K)}\sum_{i=1}^{n_g} x_h x_k w_g, \tag{29}$$

where $\mathbf{x}$ is the coordinate in an element baricentric reference system and w_g is the weight of the Gauss nodes. Following Cimarelli *et al.*,[1] the tensorial subgrid viscosity is used to model also the scalar quantities,

$$Q_i^{sgs} = -\frac{1}{2}\bar{\rho}\nu_{ih}\partial_h\tilde{T} \tag{30}$$

and

$$\tau(u_i, u_k, u_k) \simeq \tau(u_i, u_k u_k) = -\frac{1}{2}\bar{\rho}\nu_{ih}\partial_h(\tilde{u}_k\tilde{u}_k). \tag{31}$$

Now a dynamic procedure is applied. Each subgrid term is modulated by tensorial coefficient,[1]

$$\tau_{ij} = -C_{ij}\left(\nu_{kj}\partial_k\tilde{u}_i + \nu_{ki}\partial_k\tilde{u}_j\right), \tag{32}$$

$$Q_i^{sgs} = -\frac{1}{2}C_i^Q\bar{\rho}\nu_{ih}\partial_h\tilde{T}, \tag{33}$$

$$\tau(u_i, u_k u_k) = -\frac{1}{2}C_i^J\bar{\rho}\nu_{ih}\partial_h(\tilde{u}_k\tilde{u}_k). \tag{34}$$

A test filter operator $\widehat{\cdot}$ is introduced

$$\widehat{a} = \sum_{l=0}^{n_\psi(K)/2} a^{(l)}\psi_l^K \tag{35}$$

and also a Favre test filter $\breve{a} = \widehat{\rho a}/\widehat{\rho}$. The Germano identity reads

$$\mathscr{L}_{ij} = \mathscr{T}_{ij} - \widehat{\tau}_{ij} = \widehat{\bar{\rho}\tilde{u}_i\tilde{u}_j} - \widehat{\bar{\rho}}\breve{\tilde{u}}_i\breve{\tilde{u}}_j \tag{36}$$

and similarly

$$\mathscr{L}^Q_i = \mathscr{Q}^{sgs}_i - \widehat{Q}^{sgs}_i = \widehat{\bar{\rho}\tilde{u}_i\tilde{T}} - \widehat{\bar{\rho}}\breve{\tilde{u}}_i\breve{\tilde{T}}\ , \tag{37}$$

$$\mathscr{L}^J_i = \mathscr{T}(u_i, u_k u_k) - \widehat{\tau}(u_i, u_k u_k) = \widehat{\bar{\rho}\tilde{u}_i(\tilde{u}_k\tilde{u}_k)} - \widehat{\bar{\rho}}\breve{\tilde{u}}_i(\breve{\tilde{u}_k\tilde{u}_k}), \tag{38}$$

where

$$\mathscr{T}_{ij} = \widehat{\overline{\rho u_i u_j}} - \widehat{\bar{\rho}}\breve{\tilde{u}}_i\breve{\tilde{u}}_j, \tag{39}$$

$$\mathscr{Q}^{sgs}_i = \widehat{\overline{\rho u_i T}} - \widehat{\bar{\rho}}\breve{\tilde{u}}_i\breve{\tilde{T}}\ , \tag{40}$$

$$\mathscr{T}(u_i, u_k u_k) = \widehat{\overline{\rho u_i u_k u_k}} - \widehat{\bar{\rho}}\,\breve{\tilde{u}}_i(\breve{\tilde{u}_k\tilde{u}_k}). \tag{41}$$

Applying the tensorial viscosity model to the test filtered terms

$$\mathscr{T}_{ij} = -C_{ij}\widehat{\bar{\rho}}\left(\widehat{\nu}_{kj}\partial_k\breve{\tilde{u}}_i + \widehat{\nu_{ki}\tilde{u}_j}\right), \tag{42}$$

$$\mathscr{Q}^{sgs}_i = -\frac{1}{2}C^Q_i\widehat{\bar{\rho}}\widehat{\nu}_{ih}\partial_h\breve{\tilde{T}}\ , \tag{43}$$

$$\mathscr{T}(u_i, u_k u_k) = -\frac{1}{2}C^J_i\widehat{\bar{\rho}}\widehat{\nu}_{ih}\partial_h(\breve{\tilde{u}_k\tilde{u}_k}) \tag{44}$$

and assuming that the tensorial coefficients are scale invariant, we get

$$C_{ij} = \frac{\mathscr{L}_{ij}}{\mathscr{N}_{ij}}, \quad C^Q_i = \frac{\mathscr{L}^Q_i}{\mathscr{N}^Q_i}, \quad C^J_i = \frac{\mathscr{L}^J_i}{\mathscr{N}^J_i}, \tag{45}$$

where

$$\widehat{\nu}_{ki} = -\frac{1}{2}\tau(\widehat{x_h, x_k})\partial_h\breve{\tilde{u}}_i \tag{46}$$

and

$$\mathscr{N}_{ij} = \bar{\rho}\widehat{\nu_{kj}\partial_k\tilde{u}_i} + \bar{\rho}\widehat{\nu_{ki}\partial_k\tilde{u}_j} - \widehat{\bar{\rho}}\widehat{\nu}_{kj}\partial_k\breve{\tilde{u}}_i - \widehat{\bar{\rho}}\widehat{\nu}_{ki}\partial_k\breve{\tilde{u}}_j, \tag{47}$$

$$\mathscr{N}^Q_i = \widehat{\bar{\rho}\nu_{ki}\partial_k\tilde{T}} - \widehat{\bar{\rho}}\widehat{\nu}_{ki}\partial_k\breve{\tilde{T}}, \tag{48}$$

$$\mathscr{N}^J_i = \widehat{\bar{\rho}\nu_{ki}\partial_k(\tilde{u}_k\tilde{u}_k)} - \widehat{\bar{\rho}}\widehat{\nu}_{ki}\partial_k(\breve{\tilde{u}_k\tilde{u}_k}). \tag{49}$$

The tensorial coefficients computed with the dynamic procedure are averaged over the grid element, so that it can be considered independent of the applied filter. Moreover, the coefficients are clipped to get non-negative total dissipation. For a better comprehension of these two sections, let us finally briefly review again the meaning of symbols that, as usual in a dynamic procedure, could generate some confusion. The overline $\bar{\cdot}$ stands for the LES filtering operator, the tilde $\tilde{\cdot}$ stands for the associated Favre operator, while the $\widehat{\cdot}$ and $\breve{\cdot}$ represent the test filter and the associated Favre test filter, respectively. We remark that in our formalism, we do not explicitly introduce Favre fluctuations. The variable-density SGS contributions to the momentum equation are written explicitly in terms of the SGS central moments.[19] For further up to date reflections on that and more generally on the treatment of variable density turbulent flows, see Saenz *et al.*[20] and Livescu.[21]

A. Subgrid scale models selected for comparison

An attempt to take into account anisotropy of the grid element using its inertial tensor has been made also in Abbà *et al.*[10] For this reason, we refer as comparison also to the results obtained with that model, in the following called A3. We briefly recall its formulation here for completeness. In this model, a fourth order tensor B_{ijrs} is introduced,[6] which links the subgrid stresses to the strain rate tensor,

$$\tau_{ij} = -2B_{ijrs}\bar{\Delta}^2|\tilde{\mathscr{S}}|\tilde{\mathscr{S}}_{rs}. \tag{50}$$

In a locally rotated reference frame, the tensor B_{ijrs} becomes diagonal with respect to two indices. In the formulation proposed in Abbà *et al.*[10] and used here, this local reference frame is aligned with the eigenvector $\boldsymbol{\omega}_i$ of the inertial tensor of the grid element. In this way, the sgs stresses assume the following form:

$$\tau_{ij} = -\bar{\rho}|\tilde{\mathscr{S}}|\sum_{\alpha,\beta=1}^{3} C_{\alpha\beta}\bar{\Delta}_{\alpha\beta}\omega_{i\alpha}\omega_{j\beta}\omega_{r\alpha}\omega_{s\beta}\widetilde{\mathscr{S}}_{rs}, \tag{51}$$

where the tensor $\bar{\Delta}_{\alpha\beta} = (\sqrt{\lambda_i\lambda_j}n^2_\Phi(K))^{-1}$ is the function of the eigenvalues λ_i of the inertial tensor of the mesh element, and the unknown coefficients $C_{\alpha\beta}$ are determined using the Germano identity and the dynamic procedure. A similar approach is applied to the subgrid heat flux Q^{sgs}_i and to the kinetic energy flux $\tau(u_i, u_k u_k)$, which, respectively, read

$$Q^{sgs}_i = -\bar{\rho}|\tilde{\mathscr{S}}|\sum_{\alpha=1}^{3} C^Q_\alpha\bar{\Delta}_{\alpha\alpha}\omega_{i\alpha}\omega_{r\alpha}\partial_r\tilde{T}, \tag{52}$$

$$\tau(u_i, u_k u_k) = -\bar{\rho}|\tilde{\mathscr{S}}|\sum_{\alpha=1}^{3} C^J_\alpha\bar{\Delta}_{\alpha\alpha}\omega_{i\alpha}\omega_{r\alpha}\partial_r(\tilde{u}_k\tilde{u}_k/2) \tag{53}$$

and where the unknown coefficients C^Q_α and C^J_α are again computed using the dynamic procedure and are averaged in the element.

As already mentioned, in tensorial eddy viscosity models, the turbulent stress tensor is not forced to be aligned to the strain rate tensor. To highlight how this property is important to well reproduce the anisotropy character of turbulence, a comparison with a scalar eddy viscosity model is also presented in Sec. IV. To this aim, a dynamic isotropic model based on Abbà *et al.*[15] is here presented. In this model, the subgrid terms are modeled as

$$\tau_{ij} = -\bar{\rho}|\tilde{\mathscr{S}}|C_S\bar{\Delta}^2\widetilde{\mathscr{S}}_{ij}, \tag{54}$$

$$Q^{sgs}_i = -\bar{\rho}|\tilde{\mathscr{S}}|C_Q\bar{\Delta}^2\partial_i\tilde{T}, \tag{55}$$

$$\tau(u_i, u_k u_k) = -\bar{\rho}|\tilde{\mathscr{S}}|C_J\bar{\Delta}^2\partial_i(\tilde{u}_k\tilde{u}_k/2). \tag{56}$$

Here, $\bar{\Delta}$ represents the cubic root of the element volume divided by the number of degrees of freedom $n_\psi(K)$ in the element. Again, the unknown coefficients C_S, C_Q, and C_J are determined by the dynamic procedure and are averaged in the element. This isotropic dynamic model will be indicated in the following as ISO.

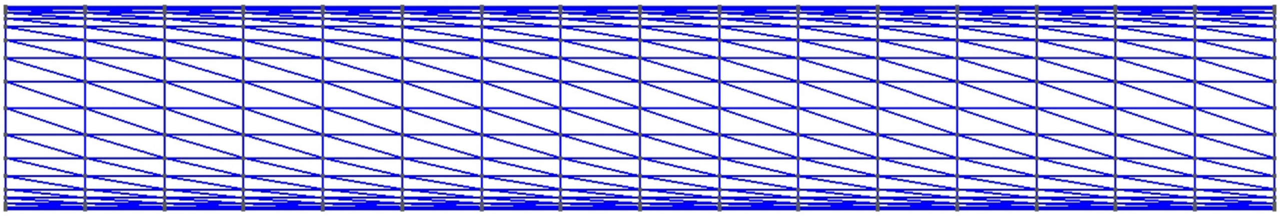

FIG. 1. Representation of the mesh used for the plane channel flow simulation with $N_x = N_y = 16$, $N_z = 12$.

IV. COMPRESSIBLE TURBULENT CHANNEL FLOW SIMULATIONS

In order to compare the performances of the described approaches, we have computed a typical LES benchmark, the compressible turbulent channel flow. Although the simplicity of the geometry of this classical test case, it represents a fundamental first test for the present model in compressible conditions. The results are compared with the data from the DNS of Wei and Pollard[22] and from the LES with the anisotropic A3 and the isotropic ISO models.

The computational domain Ω is a box of size $L_x/h = 4\pi$, $L_y/h = 2$, and $L_z/h = 4\pi/3$ in dimensionless units, and it is aligned with a reference frame, such that x represents the streamwise axis, y the wall normal, and z the spanwise axis. The bulk Reynolds number $Re_\mathrm{b} = 2795$ and Mach number $Ma_\mathrm{b} = 0.7$, which are defined as

$$Re_\mathrm{b} = \frac{\rho_\mathrm{b} U_\mathrm{b} h}{\mu_\mathrm{w}}, \quad Ma_\mathrm{b} = \frac{U_\mathrm{b}}{\sqrt{\gamma R T_\mathrm{w}}},$$

are imposed. Here, h is the half height of the channel, ρ_b and U_b are the bulk density and the bulk velocity, respectively, T_w is the wall temperature, and $\mu_\mathrm{w} = \mu(T_\mathrm{w})$ is the viscosity of the fluid at the wall.

Isothermal, no-slip boundary conditions are imposed at the walls for $y/h = \pm 1$, while periodic conditions are applied in the streamwise and spanwise directions. The simulations are initialized with a random noise superimposed to a logarithmic velocity profile in the streamwise direction, and uniform density and temperature fields. A uniform in the space body force is imposed along the streamwise direction in order to guarantee the flow rate corresponding to the desired bulk velocity. The wall shear stress τ_w, the friction Reynolds number Re_τ, and the skin friction velocity u_τ, defined as

$$\tau_\mathrm{w} = \mu_\mathrm{w}(\partial_y \langle u_x \rangle)_\mathrm{w}, \quad Re_\tau = \sqrt{\rho_\mathrm{w} Re_\mathrm{b} \frac{\tau_\mathrm{w}}{\mu_\mathrm{w}}},$$

$$u_\tau = \frac{Re_\tau}{Re_\mathrm{b} \rho_\mathrm{w}},$$

are computed *a posteriori* for each simulation, where $\langle \cdot \rangle$ stands for the Reynolds average operator.

The computational mesh is obtained by a structured mesh with N_x, N_y, and N_z hexahedra in the x, y, and z directions, respectively, each of which is then split into $N_t = 6$ tetrahedral elements. A sketch of the mesh with $N_x = N_y = 16$, $N_z = 12$ is represented in Fig. 1. While uniform in the x and z directions, the hexahedral mesh is stretched in the y direction by a hyperbolic tangent law in order to ensure a sufficient resolution of the near-wall regions. The polynomial degree for $\mathscr{V}_h$ is $p_K = 4$, resulting in $n_\psi = 35$ degrees of freedom in each element. Hence, we can define an equivalent grid spacing

$$\Delta_{x,z} = \frac{L_{x,z}}{N_{x,z} \sqrt[3]{N_t n_\psi}}, \quad \Delta_{y_i} = \frac{y_i - y_{i-1}}{\sqrt[3]{N_t n_\psi}}$$

and, in wall units, $\Delta_i^+ = Re_\tau \Delta_i$, for $i = x, y$, and z. Using the skin friction Reynolds number of the corresponding DNS, we can now determine $\Delta_{y_1} = \Delta_{y_{min}} = Re_\tau^{-1} \Delta_{y_{min}}^+$, requiring that several points are located at a distance from the wall $y^+ < 5$, so that the near-wall region is well resolved. The grid parameters are summarized in Table I. Three different resolutions have been used varying the values for N_x and N_z as reported in Table I, while the resolution in the normal to the wall direction remains unchanged. The grid corresponding to the higher resolution is the same used in Abbà *et al.*[10] and Abbà *et al.*[15] with the A3 and ISO models.

After the statistical steady state was reached, the simulations were continued for a dimensionless time (defined using h and U_b as

TABLE I. Parameters of the present simulations: reference DNS,[22] LES with the A3[10] and ISO[15] models.

	$L_x \times L_z$	$N_x \times N_y \times N_z$	DoF	Δ_x^+	Δ_z^+	$\Delta_{y_\mathrm{min}}^+/\Delta_{y_\mathrm{max}}^+$
DNS A3, ISO	12×6		3 456 0000	4.89	4.89	0.19/2.89
	$4\pi \times \frac{4}{3}\pi$	$16 \times 16 \times 12$	645 120	24	11	0.67/8.2
Present	$4\pi \times \frac{4}{3}\pi$	$16 \times 16 \times 12$	645 120	24	11	0.67/8.2
	$4\pi \times \frac{4}{3}\pi$	$12 \times 16 \times 10$	403 200	32	13.5	0.67/8.2
	$4\pi \times \frac{4}{3}\pi$	$8 \times 16 \times 8$	215 040	48	22	0.67/8.2

reference quantities) equal to 90 in order to verify time invariance of the mean profiles and to compute all the statistics. In the following, $\langle \cdot \rangle$ means average in time and in the homogeneous directions. The computational costs of performing the simulations have been found to be substantially unaltered between the different turbulence closures adopted. In particular, we measure a computational time of about 1090 core hours to simulate 60 non-dimensional times using the 96 CPUs Intel CascadeLake 8260, indifferently for all the considered models.

In Table II, the mean flow quantities at the wall are compared with the reference DNS results. The sensitivity of the results to the grid resolution is evident. The low resolution in the spanwise direction increases the size of the turbulent structures in the wall region reducing the shear wall stress. Despite this, the predicted values of wall stress and friction Reynolds number are in close agreement with the DNS results and show an improvement with respect to those obtained using the A3 and ISO models. While the mean density is always underestimated at the wall, the friction velocity is overestimated for the higher resolution. In any case, the errors with respect to the reference DNS are lower than 4% also for the lower resolution. Summarizing all the mean flow quantities presents an improvement of the present model with respect to the A3 and ISO closures.

We consider now the wall-normal profiles of the most relevant flow statistics. Figure 2 shows the mean density profiles. The solution of the present model at the high resolution is found to closely reproduce the DNS behavior. The main differences are observed for the A3 and ISO models and for the present model at a lower resolution, especially in the near-wall region where the effect of decreasing of the resolution is more relevant. The mean streamwise velocity profile expressed in wall unit is depicted in Fig. 3. Again, the mean flow solution predicted by the present model at the high resolution is found to nicely recover the DNS profile. At the lower resolution and for the A3 and ISO models, the overestimated velocity value in the center of the channel is related to the defect of the friction velocity. Overall, an improvement of the present model with respect to the A3 and ISO models is observed also in this plot.

The profiles of the mean total turbulent stresses $\langle \sigma_{ij} \rangle = \langle \tau_{ij} \rangle + \langle \rho \rangle \langle u_i' u_j' \rangle$, sum of the modeled $\langle \tau_{ij} \rangle$ plus the resolved $\langle \bar{\rho} \rangle \langle u_i' u_j' \rangle$ contributions, normalized by the wall stress τ_w, are displayed in Fig. 4. Here, $u_i' = \tilde{u}_i - \langle \tilde{u}_i \rangle$ are the resolved velocity fluctuations. As shown in the top left panel of Fig. 4, the present model at the higher resolution is found to nicely reproduce the DNS behavior for the streamwise component of the normal stress. For the other components of the normal stresses shown in the top right and bottom left panels of Fig. 4, the present model shows an improvement of the LES prediction, especially in the wall region. Indeed, the results obtained with present model at the middle resolution are very similar to those one of the A3 model with higher resolution. The normal stresses profiles recovered with the lower resolution overestimate the streamwise component of the DNS, while in other directions, stresses are under estimated. About the shear stress component, the present model shows a complete recovery of the DNS solution, even if the middle resolution is used.

TABLE II. Mean flow quantities obtained by the numerical simulations of the plane channel flow at $Re_b = 2795$ and $Ma_b = 0.7$. The present results are compared with the reference DNS[22] and with the results obtained with the A3 anisotropic model[10] and the ISO model.[15]

	τ_w	Re_τ	u_τ/U_b	ρ_w/ρ_b
DNS	12.38	186	0.0618	1.107
ISO 16 × 16 × 12	10.73	178	0.0608	1.06
A3 16 × 16 × 12	11.16	177	0.0631	1.06
Present 16 × 16 × 12	11.94	187	0.0635	1.07
Present 12 × 16 × 10	10.74	177	0.0606	1.05
Present 8 × 16 × 8	10.11	172	0.0588	1.04

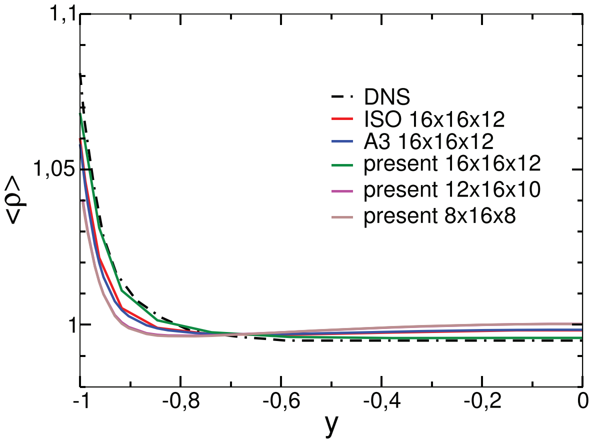

FIG. 2. Mean density profiles in the plane channel flow at $Re_b = 2795$ and $Ma_b = 0.7$.

To close the analysis of predicted turbulence fluctuations, profiles of the root mean square of temperature fluctuations are reported in Fig. 5. Again, the present model at the high resolution is found to recover the DNS behavior. The quality of the proposed modeling approach can be highlighted by noting that the present model at the lower resolution level significantly improves the prediction of

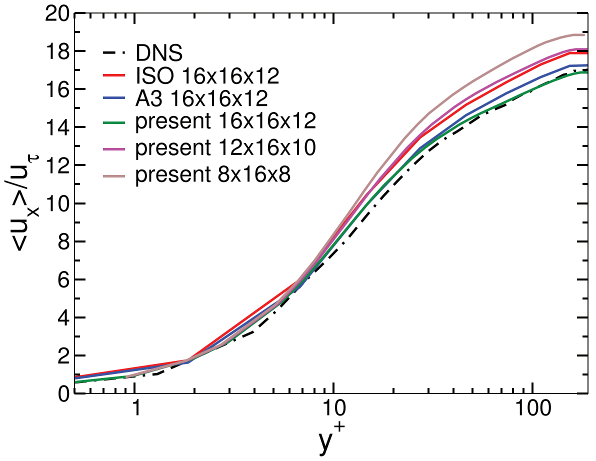

FIG. 3. Mean velocity profiles in wall units for the plane channel flow at $Re_b = 2795$ and $Ma_b = 0.7$.

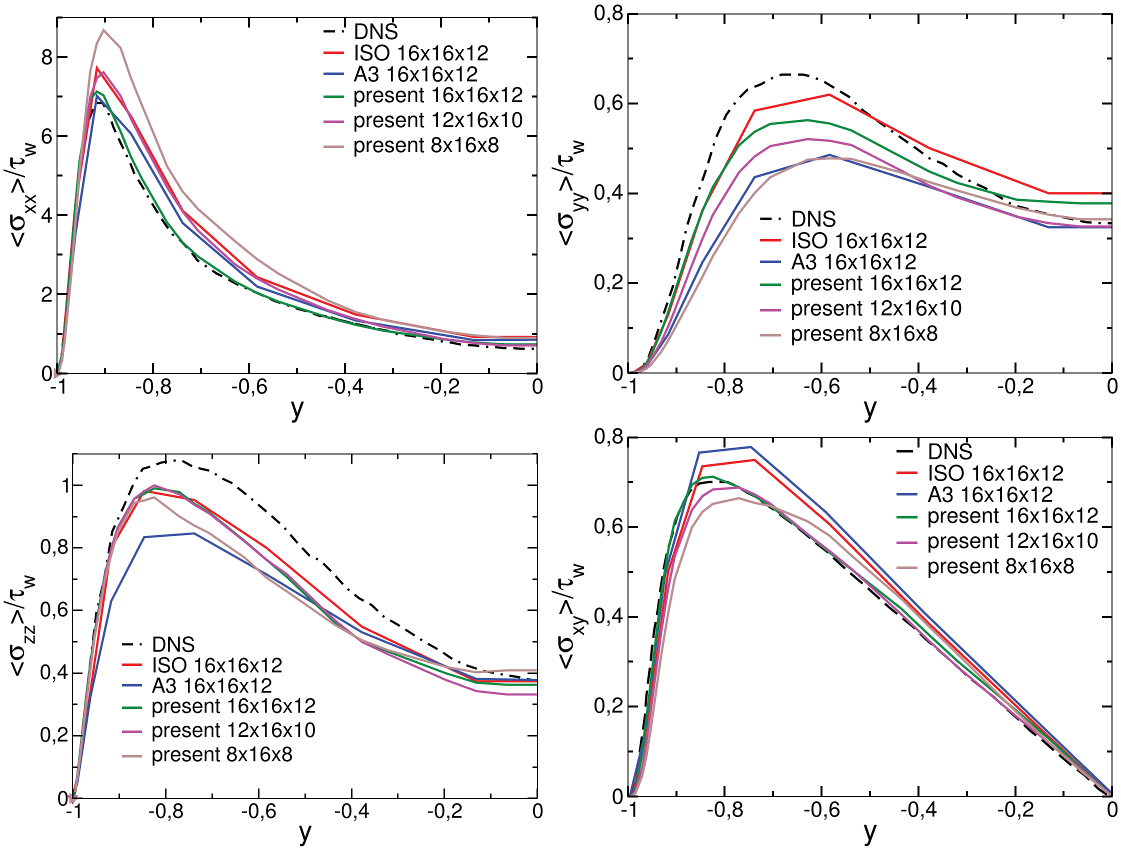

FIG. 4. Profiles of the mean total (resolved plus modeled) turbulent stresses in the plane channel flow at $Re_b = 2795$ and $Ma = 0.7$.

temperature fluctuations given by the A3 and ISO models at the highest resolution.

In order to have a more concise and quantitative view of the results described so far, the reader is referred to Table III where the average of the difference between the mean profiles obtained by LES simulations and by the DNS is reported. This difference is averaged in the y direction and is evaluated for a generic mean quantity $\langle f\rangle$ as

$$\delta f = \frac{\sum_j \left(\langle f_{LES}\rangle(y_j) - \langle f_{DNS}\rangle(y_j)\right)^2}{\sum_j \left(\langle f_{DNS}\rangle(y_j)\right)^2}. \tag{57}$$

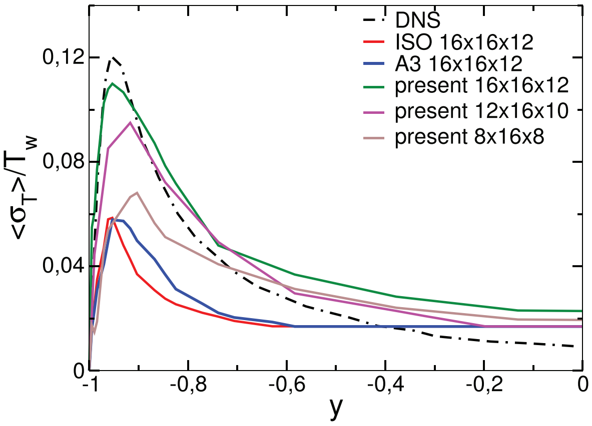

FIG. 5. Root mean square of temperature fluctuations profile, normalized by the wall temperature, in the plane channel flow at $Re_b = 2795$ and $Ma_b = 0.7$.

In closing this section, let us analyze how the turbulence anisotropy is reproduced by the present model. In Fig. 6, the turbulence barycentric map of the eingenvalues of the total turbulent stress anisotropy tensor[23]

$$\alpha_{ij} = \frac{\langle\sigma_{ij}\rangle}{\langle\sigma_{kk}\rangle} - \frac{\delta_{ij}}{3} \tag{58}$$

is reported. The map provides the possibility of characterizing any point inside it, in terms of limiting states of turbulence. In particular, the corners represent the one-component, two-component, and three-component limiting states of turbulence. The corners are joint by lines. The lower side of the triangle visualizes the two component turbulence state, while the other two sides represent the axy-symmetric contraction and expansion. The trajectories in the map move from the two components limit at the wall toward the one component corner before heading toward the isotropic three components corner in the channel

TABLE III. Mean differences between the profiles of the LES and of the reference DNS[22] represented in Figs. 2–5.

	$\delta\rho \times 10^2$	$\delta U \times 10^2$	$\delta\sigma_{xx} \times 10^2$	$\delta\sigma_{yy} \times 10^2$	$\delta\sigma_{zz} \times 10^2$	$\delta\sigma_{xy} \times 10^2$	$\delta\sigma_T \times 10^2$
ISO	1.02	1.71	14.1	5.56	14.2	11.7	54.9
A3	1.03	1.56	8.59	17.2	14.3	12.9	51.4
Present $16 \times 16 \times 12$	0.475	1.16	5.41	12.1	11.1	4.51	14.9
Present $12 \times 16 \times 10$	1.38	1.97	18.4	19.1	11.6	10.8	19.4
Present $8 \times 16 \times 8$	1.41	2.23	35.4	28.0	14.9	16.5	46.2

core. Also in this case, the present model demonstrates the capability to well reproduce the anisotropic features of the turbulent flow. Indeed, the results obtained with the higher resolution approach the DNS data better than the A3 and ISO models with the same resolution. Also in this case, the solution with the middle resolution presents a behavior similar to the A3 model.

V. PERIODIC HILL SIMULATION

The flow over periodic hills is here considered. This is an internal flow in an infinite channel constricted by a series of hills in the streamwise direction. The flow separates on the top of each hill, creating a significant turbulent recirculation bubble, and then re-attaches before the following hill, where the flow is accelerated on the forward side. This test case was introduced by Almeida *et al.*,[24] while the stretched geometry introduced by Fröhlich *et al.*[25] is used to ensure that the flow reattaches before reaching the following hill. The height of the hill is denoted by h, the total height of the channel is $L_y = 3.036h$, while the distance among the hills is $L_x = 9.0h$, and the spanwise dimension of the domain is $L_z = 4.5h$.

The simulation is performed at a Reynolds number $Re_b = 2800$, based on the bulk velocity in the channel section and on the height h of the hill, and at a Mach number $Ma_b = 0.2$ defined in a similar way. The choice of a small but not negligible Mach number is justified with the aim at comparing results with incompressible reference data. In this case, DNS data of simulations performed at this exact Mach number are available from the recent work of Balakumar and Park;[26] however, these show little or, in most cases, completely no discrepancies with the incompressible results of Breuer *et al.*[27] Since the latter are more easily available, they are used as comparison. The results are also compared with the data obtained with a LES performed employing the dynamic anisotropic model (A3) presented in Abbà *et al.*[10] The mesh, represented in the two-dimensional view in Fig. 7, is extruded in the spanwise direction leading to a total of 23 528 tetrahedra.

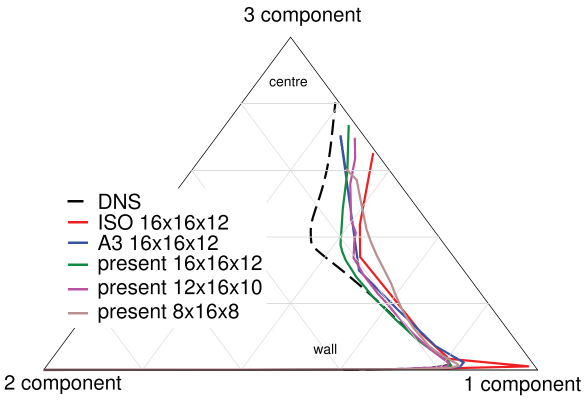

FIG. 6. Barycentric map: the anisotropy of the total, modeled plus resolved, turbulent stress tensor from the present LES is compared with the Reynolds stress tensor from the reference DNS and from LES using the A3 and ISO models.

The resolution of the lower structured region is equal to the one already used in Abbà *et al.*,[15] with the following maximum wall equivalent resolutions: $\Delta_y = 0.003\,25h$ in the wall normal direction, $\Delta_z = 0.062h$ in the spanwise direction, and $\Delta_x = 0.023h$ in the streamwise direction. The number of degrees of freedom, obtained multiplying the total number of elements by $n_\psi = 35$, and the spanwise resolution of the present simulation and of the DNS are reported in Table IV.

Periodic boundary conditions are imposed in the spanwise direction and streamwise direction. On the top and bottom walls non-slip, isothermal conditions are imposed. As done by other authors, e.g., Fröhlich *et al.*[25] and You *et al.*,[28] the mesh employed focused on the lower wall resolution, where most of the complex flow features are generated while leaving less refined the resolution at the upper wall. Although a non-slip condition with a less refined resolution is applied to the upper wall and the laminar sublayer is not well resolved there, we consider the present LES as reliable results. Indeed, it has been verified in previous tests that the differences in using no-slip or free-slip condition are significant only in a very thin layer close to the wall.

The simulation was started from a logarithmic profile with superimposed a random disturbance and then let evolve for 60 non-dimensional time units (defined using h and U_b as reference quantities) to reach statistically steady state. Subsequently, the simulations were restarted for another 60 time units to accumulate the statistics. The statistics were calculated along two different lines at $x/h = \{2.0; 4.0\}$, highlighted in Fig. 7, by averaging in the spanwise direction and in time. A simulation of 80 non-dimensional time units using 144 CPUs Intel CascadeLake 8260 required about 1500 core hours.

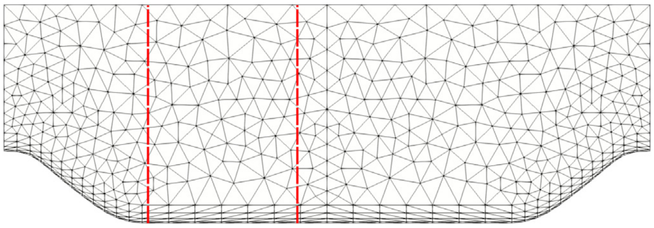

FIG. 7. Two dimensional section of the grid for the flow over periodic hills. The locations at which statistics have been recorded are highlighted by red lines.

TABLE IV. Total number of degree of freedom and grid resolution in the spanwise direction for the periodic hill flow in the LES simulation (present, A3, and ISO) and in the DNS from Balakumar and Park[26] and Breuer *et al.*[27]

	Degree of freedom	Δ_z
DNS[27]	48×10^6	0.0148
DNS[26]	38.1×10^6	0.015
LES	8.2×10^5	0.062

The profiles of mean streamwise and vertical velocity are represented in Figs. 8 and 9, respectively. The negative peak in the recirculating region and the following accelerating trend are well reproduced in the streamwise velocity profiles. Good results are observed also for the vertical velocity component, the only relevant discrepancy being given by the fact that the present model a bit overestimates the vertical velocity in the shear above the recirculating bubble, while the A3 and the ISO models underestimate it. Any other relevant differences are not evident between the LES models in these plots.

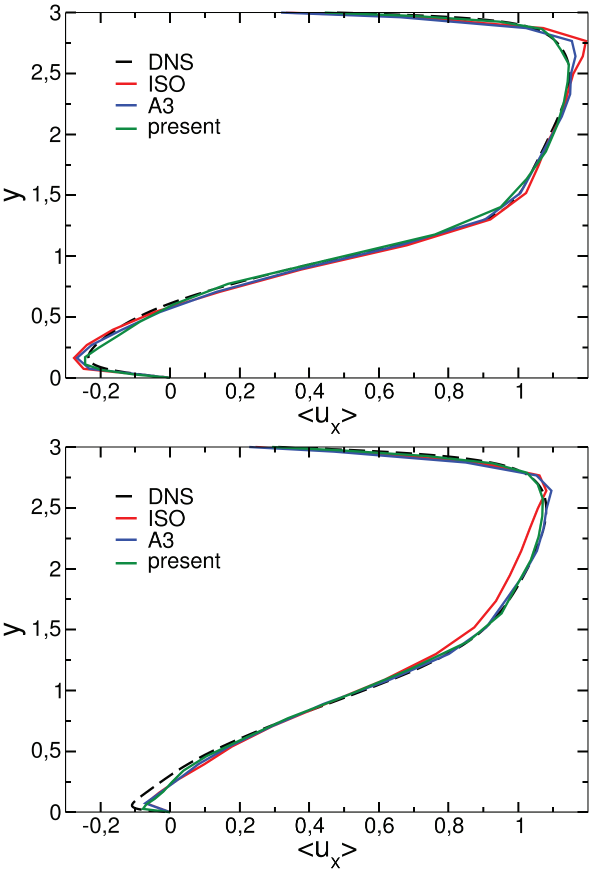

FIG. 8. Profiles of the mean longitudinal velocity component in the periodic hill flow at $x = 2$ (top) and $x = 4$ (bottom).

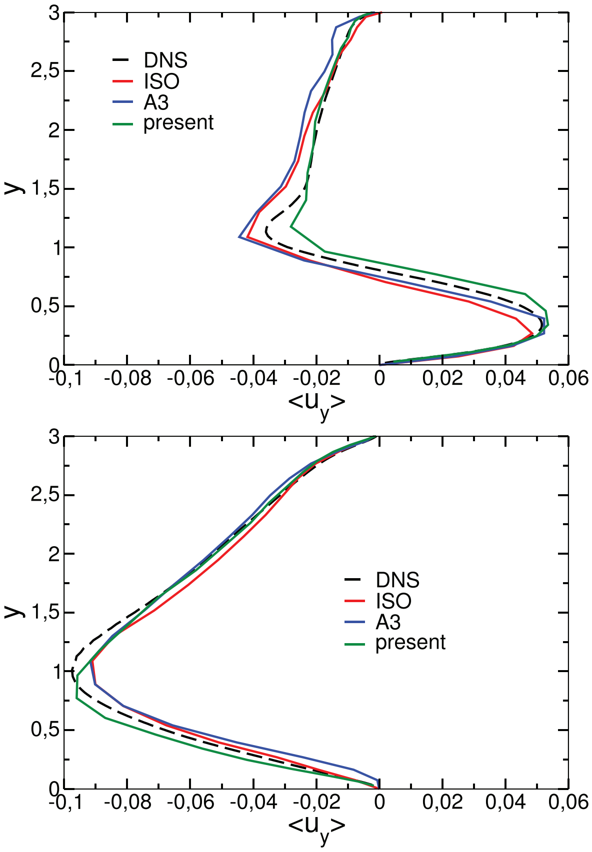

FIG. 9. Profiles of the mean vertical velocity component in the periodic hill flow at $x = 2$ (top) and $x = 4$ (bottom).

While the isotropic character of the subgrid model does not seem to affect significantly the mean velocity profiles, more relevant discrepancies are visible from total turbulent stresses reported in Figs. 10–12. Both the anisotropic models show general agreement with the DNS profiles, contrary to the isotropic approach that is found to show some limitations in reproducing the strongly inhomogeneous and anisotropic features of the flow. In particular, the present model reproduces the streamwise component of turbulent stresses better than the other two models, not only in the recirculation bubble and in the shear layer above it, but also especially in the upper half of the channel where a very low mesh resolution is adopted, see Fig. 10. The importance to take into account anisotropic character of subgrid scales manifests in the vertical component of turbulent stresses where the ISO model overpredicts the velocity fluctuations, especially in the recirculating flow, see Fig. 11. Finally, the behavior of the anisotropic models is essentially in good agreement with DNS also for the turbulent shear stresses reported in Fig. 12.

In Fig. 13, the turbulence baricentric map is shown. The baricentric map for $x = 2$ cuts through the mean flow recirculation region. The trajectory starts from the two component limit close to the lower wall where the turbulence structure is 2D axisymmetric. Then, moving away and crossing the shear layer, the trajectory moves back and forth near the 3D isotropic limit, with a small turn toward the one-component state in the shear layer above the bubble. Finally, a near

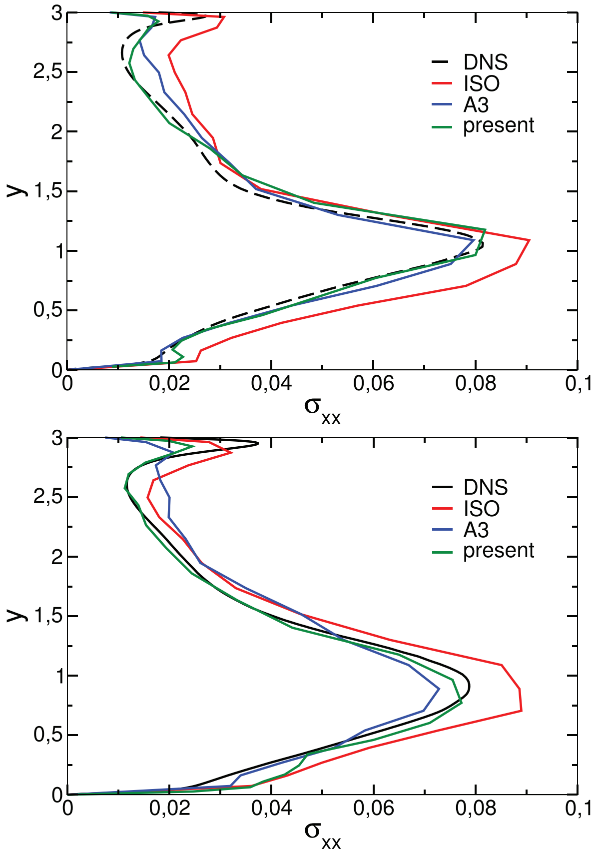

FIG. 10. Profiles of the mean total (resolved plus modeled) turbulent stresses in the periodic hill flow. Normal component in the streamwise direction of turbulent stresses, $\langle \sigma_{xx} \rangle / (\rho_b U_b^2)$, at $x = 2$ (top) and $x = 4$ (bottom).

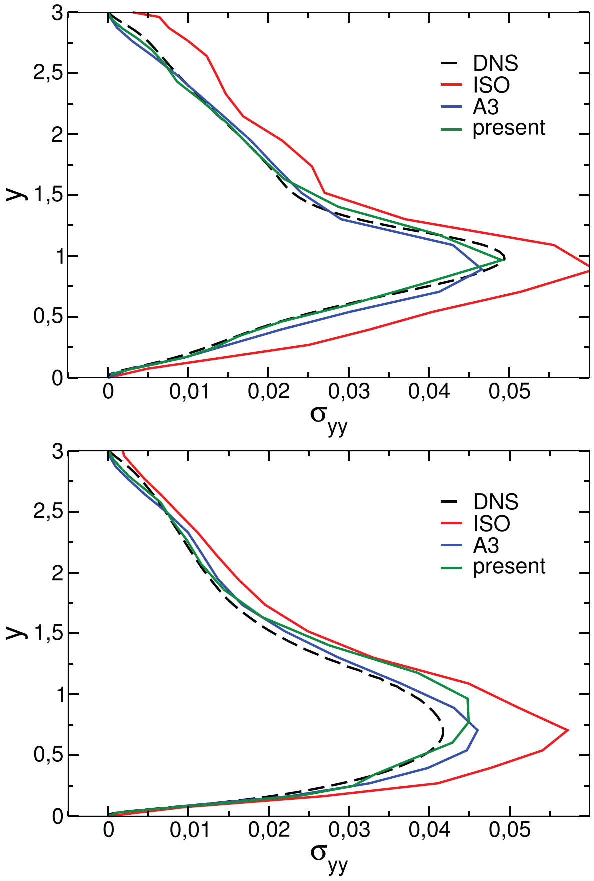

FIG. 11. Profiles of the mean total (resolved plus modeled) turbulent stresses in the periodic hill flow. Normal component in the vertical direction of turbulent stresses, $\langle \sigma_{yy} \rangle / (\rho_b U_b^2)$, at $x = 2$ (top) and $x = 4$ (bottom).

axisymmetric-expansion is present close to the upper wall approaching the one-component state. Also, the turbulence characteristic for $x = 4$, still in the main recirculation, starts from the two-component limit in the bottom wall boundary layer. Then, the trajectory progresses through the axisymmetric expansion reaching the isotropic limit in the center of the channel. Finally, an axisymmetric contraction carries the turbulence toward the area of high anisotropy in the region of the one component limit close to the upper wall. In both these baricentric maps for $x = 2$ and $x = 4$, the two anisotropic models well reproduce the behavior of the DNS trajectory, while the ISO model presents a confused path where axy-symmetric expansions and contraction are not recognizable. These baricentric maps confirm that the scalar eddy viscosity model is not suitable to adequately represent the anisotropicity of turbulence structures in such complex flows. Instead, the two tensorial eddy viscosity models well reproduce the anisotropic character of turbulence in good agreement with DNS results.

VI. CONCLUSION

Based on the formalism of the generalized central moments introduced by Germano,[18] algebraic rules that relate resolved quantities to turbulent stresses at different levels defined by a filtering procedure can be derived. Such algebraic relations, together with exact relations between generalized central moments and the two-point velocity increment,[29] have been employed in Cimarelli *et al.*[1] to derive a new class of turbulence closures in large eddy simulation. The formalism of the models is based on a tensorial turbulent viscosity, which depends on the filtered velocity gradients and on the second-order inertial properties of the grid element. The basic idea is that the anisotropic structure of the computational element directly impacts, although implicitly, the definition of large resolved and small unresolved scales. Hence, such information can be used in turbulence closures to take into account the anisotropic structure of turbulent stresses at the subgrid level. The degree of generality of the formalism is such that it can also be used to give a reduced description of subgrid scalar fluxes. This rigorous theoretical framework is finally coupled with a dynamic tensorial procedure in order to obtain optimal results also in the case of very complex flows.

In the present work, we have assessed this class of turbulence closures reported in Cimarelli *et al.*[1] by addressing their performance both in compressible conditions and in complex flows with curvature. To this aim, a compressible turbulent channel at the bulk Reynolds number $Re_b = 2795$ and Mach number $Ma_b = 0.7$ and a turbulent flow over periodic hills at $Re_b = 2800$ and $Ma_b = 0.2$ has been

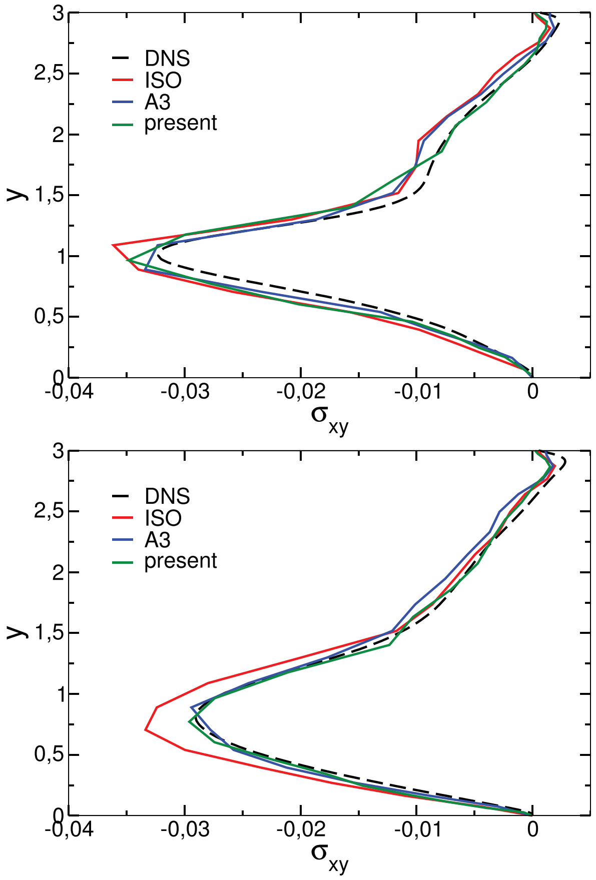

FIG. 12. Profiles of the mean total (resolved plus modeled) turbulent stresses in the periodic hill flow. Turbulent shear stresses, $\langle \sigma_{xy} \rangle/(\rho_b U_b^2)$, at $x = 2$ (top) and $x = 4$ (bottom).

considered. The comparison with DNS highlights how the present formulation accurately captures the anisotropic physics of the two flows considered also for the lower grid resolutions. Compared to the isotropic approach provided by a scalar eddy viscosity, the present anisotropic formulation based on tensorial eddy viscosity is found to significantly improve the simulation results. The comparison of the present formulation with an anisotropic model proposed by Abbà *et al.*[10] reveals an improvement in the modeling approach. In particular, the present formulation at a lower resolution is shown to perform similarly to the modeling approach proposed by Abbà *et al.*[10] at a higher resolution.

In conclusion, the generality of the formalism allows for a unified description of both subgrid stresses and fluxes and for a rigorous definition of subgrid quantities in complex flows independently of the discretization technique. Accurate results have been measured in compressible conditions and in a complex flow geometry. Hence, we believe that the present class of turbulence closures is very promising for the application of the Large Eddy Simulation technique to the solution of complex problems typical of industry and geophysics.

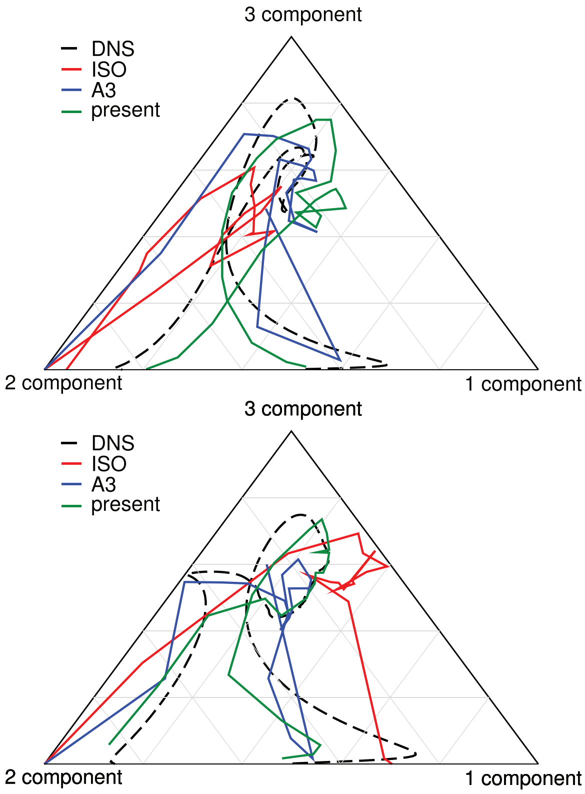

FIG. 13. Baricentric map for the periodic hill flow at $x = 2$ (top) and $x = 4$ (bottom).

ACKNOWLEDGMENTS

We acknowledge that the results of this research have been achieved using the CINECA resources made available by the high-performance computing projects under ISCRA-C HP10CGORK5.

AUTHOR DECLARATIONS

Conflict of Interest

The authors have no conflicts to disclose.

DATA AVAILABILITY

The data that support the findings of this study are available from the corresponding author upon reasonable request.

REFERENCES

[1] A. Cimarelli, A. Abbà, and M. Germano, "General formalism for a reduced description and modelling of momentum and energy transfer in turbulence," J. Fluid Mech. **866**, 865–896 (2019).

[2] J. Boussinesq, *Essai Sur la Théorie Des Eaux Courantes* (MéMoires Des Savants Etrangers, l'Académie des Sciences, Paris, 1877).

[3] J. Smagorinsky, "General circulation experiments with the primitive equations: I. The basic experiment," Mon. Weather Rev. **91**, 99–162 (1963).

[4] M. Germano, U. Piomelli, P. Moin, and W. H. Cabot, "A dynamic subgrid-scale eddy viscosity model," Phys. Fluids **3**, 1760–1765 (1991).

[5] P. Sagaut, *Large Eddy Simulation for Incompressible Flows: An Introduction*, 3rd ed. (Springer Verlag, 2006).

[6] A. Abbà, C. Cercignani, and L. Valdettaro, "Analysis of subgrid scale models," Comput. Math. Appl. **46**, 521–535 (2003).

[7] U. Schumann, "Subgrid scale model for finite difference simulations of turbulent flows in plane channels and annuli," J. Comput. Phys. **18**, 376–404 (1975).
[8] S. Zahrai, F. Bark, and R. Karlsson, "On anisotropic subgrid modeling," Eur. J. Mech. B, Fluids **14**, 459–486 (1995).
[9] J. Bardina, J. Ferziger, and W. Reynolds, "Improved subgrid scale models for large eddy simulation," AIAA Paper No. 80-1357, 1980.
[10] A. Abbà, D. Campaniello, and M. Nini, "Filter size definition in anisotropic subgrid models for large eddy simulation on irregular grids," J. Turbul. **18**, 589–610 (2017).
[11] S. Haering, M. Lee, and R. Moser, "Resolution-induced anisotropy in large-eddy simulations," Phys. Rev. Fluids **4**, 114605 (2019).
[12] M. Tugnoli, A. Abbà, L. Bonaventura, and M. Restelli, "A locally p-adaptive approach for large eddy simulation of compressible flows in a DG framework," J. Comput. Phys. **349**, 33–58 (2017).
[13] B. Cockburn and C. Shu, "The Runge–Kutta discontinuous Galerkin method for conservation laws V: Multidimensional systems," J. Comp. Phys. **141**, 199–224 (1998).
[14] F. van der Bos and B. Geurts, "Computational error-analysis of a discontinuous Galerkin discretization applied to large-eddy simulation of homogeneous turbulence," Comput. Methods Appl. Mech. Eng. **199**, 903–915 (2010).
[15] A. Abbà, L. Bonaventura, M. Nini, and M. Restelli, "Dynamic models for large eddy simulation of compressible flows with a high order DG method," Comput. Fluids **122**, 209–222 (2015).
[16] M. Pino Martìn, U. Piomelli, and G. Candler, "Subgrid-scale models for compressible large-eddy simulations," Theor. Comput. Fluid Dyn. **13**, 361–376 (2000).
[17] B. Vreman, B. Geurts, and H. Kuerten, "Subgrid-modeling in LES of compressible flow," Appl. Sci. Res. **54**, 191–203 (1995).
[18] M. Germano, "Turbulence: The filtering approach," J. Fluid Mech. **238**, 325–336 (1992).
[19] G. S. Sidharth and G. V. Candler, "Subgrid-scale effects in compressible variable-density decaying turbulence," J. Fluid Mech. **846**, 428–459 (2018).
[20] J. A. Saenz, D. Aslangil, and D. Livescu, "Filtering, averaging, and scale dependency in homogeneous variable density turbulence," Phys. Fluids **33**, 025115 (2021).
[21] D. Livescu, "Turbulence with large thermal and compositional density variations," Annu. Rev. Fluid Mech. **52**, 309–341 (2020).
[22] L. Wei and A. Pollard, "Direct numerical simulation of compressible turbulent channel flows using the discontinuous Galerkin method," Comput. Fluids **47**, 85–100 (2011).
[23] S. Banerjee, R. Krahl, F. Durst, and C. Zenger, "Presentation of anisotropy properties of turbulence, invariants versus eigenvalue approaches," J. Turbul. **8**, N32 (2007).
[24] G. P. Almeida, D. F. Durão, and M. V. Heitor, "Wake flows behind two-dimensional model hills," Exp. Therm. Fluid Sci. **7**, 87–101 (1993).
[25] J. Fröhlich, C. Mellen, W. Rodi, L. Temmerman, and M. Leschziner, "Highly resolved large-eddy simulation of separated flow in a channel with streamwise periodic constrictions," J. Fluid Mech. **526**, 19–66 (2005).
[26] P. Balakumar and G. Park, "DNS/LES simulations of separated flows at high Reynolds numbers," in *45th AIAA Fluid Dynamics Conference* (American Institute of Aeronautics and Astronautics, 2015).
[27] M. Breuer, N. Peller, C. Rapp, and M. Manhart, "Flow over periodic hills—Numerical and experimental study in a wide range of Reynolds numbers," Comput. Fluids **38**, 433–457 (2009).
[28] D. You, S. T. Bose, and P. Moin, "Grid-independent large-eddy simulation of compressible turbulent flows using explicit filtering," in *Proceedings of the 2010 Center for Turbulence Research Summer Program* (Center for Turbulence Research, 2010), pp. 203–210.
[29] M. Germano, "A direct relation between the filtered subgrid stress and the second order structure function," Phys. Fluids **19**, 038102 (2007).